Multi-parameter imaging of in-cylinder processes during transient engine operation for the investigation of soot formation

Christian Fach[1] , Nico Rödel[2], Jürgen Schorr[3], Christian Krüger[3], Andreas Dreizler[1] and Benjamin Böhm[1]

Abstract

Transient engine operation of direct-injection spark ignition engines can result in high particulate number emissions. To investigate the causes of soot formation, an engine test rig was developed to perform detailed measurements of real transient operation. For this purpose, a single-cylinder full-metal engine with a real combustion chamber geometry was equipped with minimally invasive optical accesses. Simultaneous high-speed endoscopic PIV, spray visualization, and combustion imaging were applied to investigate the in-cylinder processes in detail. Endoscopic PIV was first compared in the central symmetry plane with classical PIV performed at the equivalent optical engine at steady-state operation for verification. Then the engine parameters of a tip-in performed by the corresponding four-cylinder engine, which led to high particle number emissions, were applied to the single-cylinder engine. The engine parameters were in a good agreement and particle number emissions due to the maneuver were within the same range of several 10^6 #/cm^3. In total, 19 repetitions of the tip-in maneuver were analyzed with respect to the in-cylinder processes and repeatability of engine parameters. Furthermore, the in-cylinder flow field during the late compression stroke, flame propagation, and soot luminosity of single cycles during the tip-in indicated cause-and-effect chains for the formation of pool fire and soot at the injector tip. The direction of the flow below the spark plug influenced the direction of flame propagation. An early arrival of the flame enhanced the formation of soot from fuel films formed on the piston surface or at the injector. In engine applications, counter measures can be applied to reduce the particle number emissions when accounting for these indicated cause-and-effect chains.

Introduction

Particulate number emissions from direct-injection spark ignition (DISI) engines are regulated by legislation under the EURO 6 standard[1] and are expected to be further tightened under the EURO 7 standard. In addition, new test procedures have been introduced that represent more realistic driving conditions, such as the Worldwide Harmonized Light-duty vehicles Test Procedure (WLTP) and real driving emissions.[2] This poses a major challenge for engine development, as transient engine operation can lead to a significant increase in pollutant emissions.

Load changes, such as acceleration from idle or for a cold engine, can cause an increase in gaseous and particulate number emissions.[3–5] An emission-critical maneuver is a positive load step starting from motored engine operation, also called tip-in. Since the combustion chamber surfaces cool down during motored operation, wall wetting and as a result soot formation are

[1]Fachgebiet Reaktive Strömungen und Messtechnik, Technische Universität Darmstadt, Darmstadt, Germany
[2]Mercedes-Benz AG, Kirchheim Unter Teck, Germany
[3]Mercedes-Benz AG, Stuttgart, Germany

Corresponding author:
C Fach, Fachgebiet Reaktive Strömungen und Messtechnik, Technische Universität Darmstadt, Otto-Berndt-Str. 3, Darmstadt 64287, Germany.
Email: fach@rsm.tu-darmstadt.de

likely to happen during the load step. Sabathil et al.[6] investigated the particulate number emissions in the exhaust of a DISI engine with respect to variations of engine parameters over time. They found that a load-step causes significantly more particulate emissions than the corresponding steady-state operation. An increase of particulate number emissions during transient engine operation was also found by Boulouchos and Kirchen.[7] They compared the emissions of a tip-in and steady-state operation in an internal combustion engine. Hadler et al.[8] found a split injection strategy to reduce particulate emissions during steady-state operation. However, this strategy resulted in increased particulate emissions when applied to a tip-in. From this they derived a higher sensitivity of the injection strategy to variations of the engine parameters, which led to the increase in emissions. Since soot formation and particulate emissions exhibit cycle-to-cycle variations, techniques for cycle-resolved measurements are needed for further investigations.[9]

During transient engine operation, cycle-to-cycle variations (CCV) overlap with the effects of transients resulting in variations from transient-to-transient. Thus, the in-cylinder processes, such as in-cylinder flow, injection, and flame propagation during transient operation, are subject to transient-to-transient variations. CCV have been investigated in SI engines for a long time.[10] For a detailed analysis of cause-and-effect chains, time-resolved optical measurement techniques have proven to be useful.[11] Stiehl et al.[12] for example have investigated the interaction between the in-cylinder flow and spray formation using a high-speed particle image velocimetry (PIV) setup and observed the impact of the flow on CCV in DISI engines under steady-state operation. In a further work, Bode et al.[13] identified flow field fluctuations which correlated significantly with fluctuations of the indicated mean effective pressure (IMEP). However, for transient engine operation, the in-cylinder processes were hardly investigated experimentally. In optically accessible research engines, the in-cylinder flow field was investigated during single parameter transients of intake pressure and engine speed.[14] In a full-metal engine, Disch et al.[15] investigated soot formation via endoscopic imaging of soot luminosity during a tip-in at constant engine speed. They found the probability density of soot luminosity and its area within the combustion chamber to vary with changes in start of injection.

Optically accessible engines are often used to investigate in detail specific engine phenomena[12,13,16] or to collect data for the validation of simulations.[17–19] Optical engines represent the flow field as well as the early phase of combustion reasonably well. However, they can differ strongly from real engines with respect to in-cylinder pressure traces during combustion and pollutant emissions.[20] On the one hand, this is due to the large-area optical accesses which show a changed heat transfer. This leads to higher surface temperatures[21] and a shorter ignition delay.[22] Additionally, the typically deeper top land, which prevents the piston rings from scratching the windows, leads to a delayed combustion, since the fresh gas from the top land is only slowly released during expansion.[22] It further leads to a lower temperature and pressure at time of ignition due to a decreased compression ratio. For this reason, engines with minimally invasive optical accesses are essential for studying in-cylinder pollutant formation. They also extend the accessible load range, which is typically very limited in optical engines.

The feasibility of endoscopic PIV for the detection of flow fields was shown in different applications like an enclosed rotor-stator system,[23] a bulb turbine runner,[24] and lab-scale flameless mild combustion pilot furnace.[25] Endoscopic PIV allows further in-cylinder flow field measurements with near-production geometries.[26] Dierksheide et al.[27] showed the feasibility by comparing standard PIV with endoscopic PIV in a multi-cylinder SI engine. Goschütz et al.[28] used a large-aperture endoscope to investigate flame propagation in a near-production engine. Endoscopic imaging was used by Schueck et al.[29] to localize diffusion flames within the cylinder and by Disch et al.[15] to measure soot luminosity and to identify inhomogeneities in mixture formation during transient engine operation.

In this work, a single-cylinder DISI engine test rig is presented, which was designed to investigate the emission behavior of a near-production engine. The aim was to investigate the in-cylinder processes and their interactions within the engine that lead to increased particulate emissions during transient engine operation. The developed endoscopic engine is comparable to the corresponding four-cylinder engine in concerns of thermodynamics, soot formation and performance of transient engine operation. Its optical accessibility enables measurements of the in-cylinder processes similar to optical engines. For this purpose, simultaneous endoscopic PIV, spray, and combustion visualization via minimally invasive optical accesses were applied to the engine with real combustion chamber geometry and the investigation of a tip-in maneuver is presented.

Experimental set up

Engine

Endoscopic engine. The investigations were conducted in a single-cylinder DISI engine with a pre-series combustion chamber geometry with a bore and stroke of 78 mm. The engine was equipped with a four-valve cylinder head. A six-hole injector (Bosch HDEV 6) was placed in the central symmetry plane and the spark plug was located between the exhaust valves. The pre-series piston was equipped with real piston rings and had a top land height of 7 mm. The liner was lubricated with engine oil guided through the piston. The cylinder head and the liner were water cooled. Further engine specifications are given in Table 1.

Table 1. Specifications of the endoscopic engine.

Bore	78 mm
Stroke	78 mm
Compression ratio	10.1
Coolant temperature	85°C
Oil temperature	55°C
Fuel	Gasoline E10
Injection pressure	350 bar

Table 2. Engine parameters for the endoscopic and optical engine for the verification measurements.

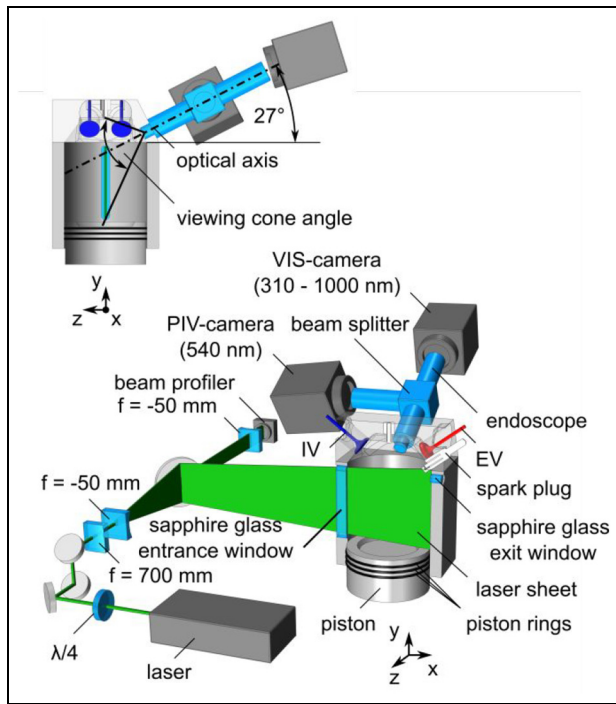|	
Engine speed	1500 rpm
Intake manifold pressure	750 mbar
Intake valve opening (2 mm valve lift)	32.5°CAaTDC
Exhaust valve closing (2 mm valve lift)	10°CAaTDC
Start of injection	−290°CAaTDC

Figure 1. Experimental setup and side view of endoscopic engine.

The cylinder head was equipped with an endoscopic access with a diameter of 12 mm between the intake valves (IV) and exhaust valves (EV) as shown in Figure 1. The cylinder liner was equipped with two sapphire windows along the central symmetry plane. One window with a height of 70 mm and a width of 8 mm between the intake valves was used as optical access for the laser sheet for PIV. The other sapphire glass window with a diameter of 8 mm at the opposite combustion chamber wall served for laser alignment purposes. The glass windows were flush-mounted with the cylinder wall and honed together with the cylinder. The honing structure was then removed as far as possible from the sapphire glass windows through polishing. This ensured that the oil was sufficiently well scraped off the windows by the piston rings that ran over the windows and enabled the laser to pass through.

To enable transient engine operation, a throttle was used to control the intake manifold pressure and thus set the real pressure gradients of the intake manifold pressure during transients. The pressure inside the air plenum upstream of the throttle was set to 1200 mbar for all measurements. For the PIV measurements, silicon oil droplets (mean diameter of 0.5 μm) were seeded (Palas AGF 10.0D) in the intake flow through two jet-in-crossflow arrangements positioned opposite of each other in the intake pipe downstream the throttle. The varying seeding density during the transients was compensated by an electric proportional needle valve (response time of 20 ms), which controlled the mass flow through the seeder. A further air plenum between the seeding feed and combustion chamber ensured homogeneous mixing of the seeding in the intake air.

Valve timing and valve lift were controlled using a hydraulic active valve train (Lotus AVT). Engine parameters were set on a time scale for each individual cycle using a parametric table also including triggers for synchronization of the cameras and laser.

Optical engine. To verify the endoscopic PIV measurements within the endoscopic engine, classical PIV measurements were performed on a corresponding single-cylinder optically accessible engine which was based on the identical engine design. The experimental set-up including the optical engine and the classical PIV was already presented in Hanuschkin et al.[30] The main differences to the endoscopic engine were the large-area optical accesses through the piston window and a 35 mm high liner made of quartz glass. The optical engine is used as reference for evaluating the PIV measurement quality during intake and compression stroke, such that the differing thermodynamics are negligible. The intake manifold pressure is controlled using a mass flow controller upstream of the air plenum. The throttle is replaced with a tube and hence pressure oscillations develop due to reflections at the connection of the tube and plenum.

Operational conditions. For the comparison between endoscopic and classical PIV the same steady-state operating point was run on both engines. The engines were operated in a homogeneous charge mode with an air-fuel-equivalence ratio of 1 and an engine speed of 1500 rpm. The engine parameters are listed in Table. Time of ignition was controlled to keep 50% mass fraction burned (MFB) constant at around 7°CAaTDC. Crank angle based engine parameters are referred to
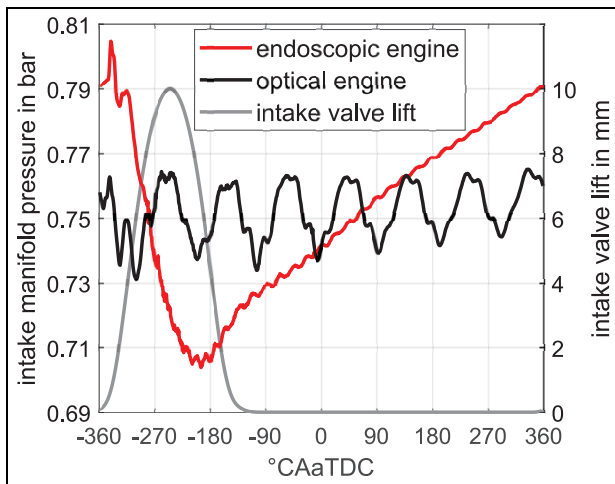
Figure 2. Intake manifold pressure of endoscopic and optical engine and intake valve lift of a single cycle.

Figure 3. Schematic drawing of the trigger signals.

top dead center (TDC) of ignition except for valve timings which are referred to TDC of gas exchange. At least 150 cycles were acquired for the comparison, which is a sufficient number of cycles for converged statistics.[18] Figure 2 shows the intake manifold pressure traces of endoscopic and optical engine together with the intake valve lift for a single cycle. Differences in the evolution of the intake manifold pressure are due to the throttle used at the endoscopic engine, which damps the pressure oscillation in the intake manifold and reduces the mass flow of fresh air during the intake stroke.

The selection of the transient operation of the endoscopic engine was part of the investigation. Details are given in section 3.2.

Endoscopic PIV and imaging

A multi-parameter endoscopic imaging approach was developed for the investigation of transient engine operation. The approach included endoscopic high-speed PIV to gain information on the evolution of the in-cylinder flow as well as high-speed imaging of the spray, chemiluminescence, and soot luminosity. The measurement principle and experimental setup of classical PIV are summarized by Adrian.[31] An analysis on the perspective error by using endoscopic imaging for PIV was performed by Reeves and Lawson.[32] They found the perspective error can be significantly reduced by using stereoscopic imaging. Since stereoscopic PIV would require two spatially separated optical accesses, it was not applied within this work due to the spatial limitations at the cylinder head of the full-metal engine. Instead, endoscopic PIV was evaluated and the influence of the perspective error was assessed.

The experimental setup is shown in Figure 1. An endoscope specially designed for the combustion chamber geometry was used for detection, which is shown schematically in Figure 1. The endoscope had a diameter
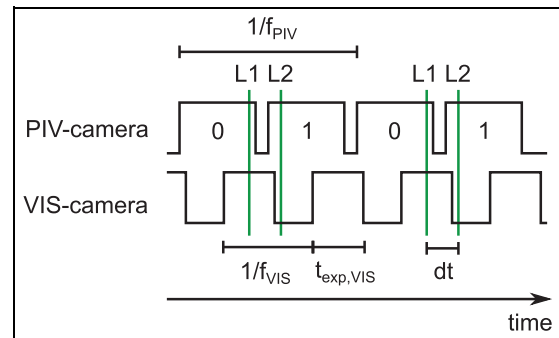
of 12 mm on the combustion chamber side and was fixed to the cylinder head. Locating pins in the cylinder and endoscope holder ensured reproducible positioning. A beam splitter with a maximum reflectivity of 90% in the middle of the endoscope reflected light in the wavelength range of 540 nm ± 60 nm towards the PIV-camera and transmitted the remaining light in the range of 300–1000 nm towards the VIS-camera. The endoscope was mounted at an angle of 27° to the horizontal plane. A Scheimpflug arrangement was realized, such that both cameras were focused on the central symmetry plane. With a viewing cone angle of 74° the resulting field-of-view (FOV) was an ellipsoid with a height of 79 mm and a width of 70 mm, which is given by the intersection of the cone of vision with the central symmetry plane. The magnification close to the cylinder head (y = 0 mm) was 0.3 and decreased to 0.1 towards the piston (y = −60 mm). Figure 3 shows a schematic drawing of the trigger signals for synchronization of the cameras and the laser pulses (L1 and L2).

Chemiluminescence and soot luminosity. The VIS-camera (Phantom v1611, color) was operated at $f_{VIS} = 11.2$ kHz providing an image every 0.8° CA at 1500 rpm. The exposure time was set to $t_{exp,VIS} = 70 \mu s$ which gives the temporal resolution of chemiluminescence and soot luminosity imaging. The depth of field along the optical axis was calculated via the endoscope specifications of the manufacturer and was about 20.1 mm for the VIS-camera.

PIV and spray. For illumination of the seeding particles used for PIV and the spray the beam of a frequency doubled dual-cavity Nd:YVO₄ laser (Edgewave, 532 nm, 0.7 mJ/pulse) was formed into a light sheet by the combination of a cylindrical concave lens ($f = -50$ mm), a spherical lens ($f = 700$ mm) and the concave sapphire glass entrance window ($f \sim -50$ mm). The laser sheet 65 mm in height and ~330 μm thick was used to illuminate the central symmetry plane. A quarter-wave plate was placed in front of the laser exit to reduce the dependency of light scattering on the polarization of the laser light.
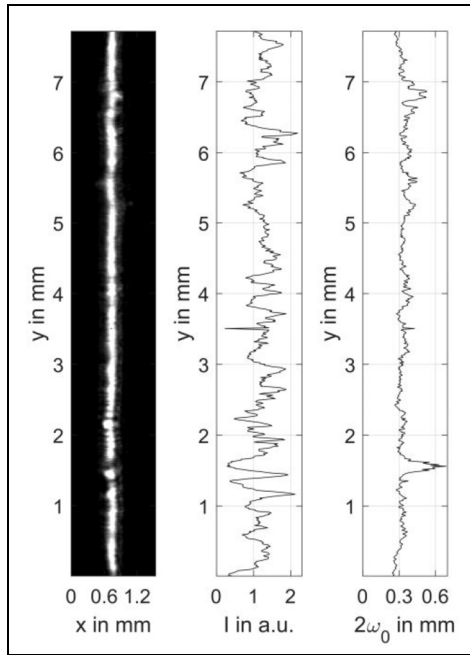
Figure 4. Laser sheet profile in the middle of the combustion chamber (left), profile of the laser intensity *I* along the center line at *x* = 0.74 mm (middle) and laser sheet thickness $2\omega_0$ (right).

A proper alignment of the laser within the engine with pre-production geometry is challenging. For a basic alignment of the laser sheet, similar to optically accessible engines, the cylinder head was unmounted and customized targets were placed in the combustion chamber. When the cylinder head was reinstalled, additional customized targets were used to check the laser position and angle at the entrance window, the middle of the combustion chamber and at the end of the combustion chamber through the small sapphire glass exit window. To adjust the beam overlap of the two laser cavities, the beam profile was measured in the near and far field using a beam profiler (DataRay WinCamD). As the cylinder head was removed the beam profiler was positioned in the middle of the combustion chamber. To check and readjust the beam overlap with the cylinder head installed, a plano-concave lens of approximately the same focal length as the sapphire glass entrance window was positioned in the straight path of the last mirror so that the resulting beam profile corresponded to that inside the engine.

Figure 4 (left) shows a representative part of the laser sheet profile measured with the beam profiler in the middle of the combustion chamber. The production-related honing structure on the sapphire glass windows was removed by polishing. Nevertheless, some cracks remained in the sapphire glass window which partially lead to a reduction of the laser intensity. This is also evident from the profile of the laser intensity *I* along the center line of the laser sheet at *x* = 0.74 mm in Figure 4 (middle). Figure 4 (right) shows the laser sheet thickness $2\omega_0$ along the measured laser sheet profile. The average laser sheet thickness is about $2\omega_0 = 330\,\mu m$ and

significant variations can only be seen in case of larger cracks in the sapphire glass.

For PIV, the scattered laser light from silicon oil droplets ($\sim$1 μm in diameter) used for seeding was focused on the PIV-camera (Phantom v1611). The PIV measurements were performed in double-frame mode at f_{PIV} = 5.6 kHz resulting in a temporal resolution of 1.6° crank angle (CA) at 1500 rpm. The laser pulse separation dt was adjusted for each engine operation and for various crank angle ranges, and it varied between 8 and 48 μs. The temporal resolution of the spray visualization of 1.6°CA was given by the repetition rate of a single cavity of the PIV laser which was used for spray illumination. For the detection path of the PIV-camera, a much smaller depth of field was aimed in order to provide focused images of a large area of the combustion chamber. The depth of field along the optical axis was around 3.9 mm.

Due to engine displacements during transient engine operation and engine vibrations, all components, endoscope, cameras, and engine were firmly connected to each other to avoid relative movements of individual components. Furthermore, a mass balance on the crank case was adapted to minimize engine vibrations.

PIV processing

For PIV processing the commercial software DaVis 8.4.3 (LaVision) was used. First, a distortion correction was performed using a calibration target positioned in the central symmetry plane. For this purpose, the endoscope had to be disassembled and the cylinder head removed. Locating pins in the cylinder and endoscope holder ensured a reproducible positioning of the endoscope. The spark plug in the images was used to check the position. In the case of shifts of individual pixels between the target image and the current measurement, a corresponding linear shift was first performed before the distortion correction was carried out using the target image. A pinhole camera model was used due to the angle of the optical axis towards the imaging plane.[33,34] The resolution was about 0.11 mm/pixel. In combination with the laser pulse separations this resulted to a theoretically resolvable velocity range of about 1–110 m/s.[35]

Figure 5 (left) shows a particle image after distortion correction. At the left and right border of the image direct reflections from the cylinder wall and a strong reflection from the piston surface were visible. Scattered light from the seeding particles reflected by the combustion chamber surfaces further reduced the image contrast. Therefore, the image contrast depended on the piston position and the seeding density, respectively. An enhanced image contrast decreases the uncertainty of the particle image position.[36] To compare the particle images before and after the preprocessing, the root-mean-square contrast[37] was calculated, given by
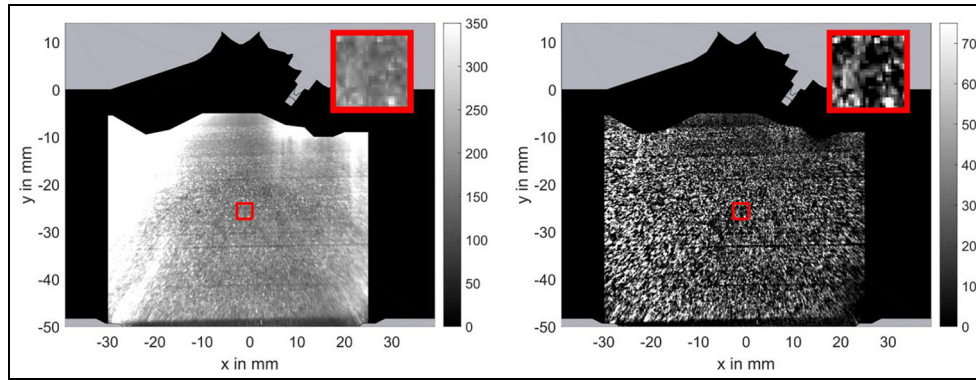
Figure 5. Distortion corrected particle image (left); particle image after preprocessing (right). The gray value intensities are shown according to the colorbars.

$$C_\sigma = \sqrt{\frac{1}{N-1} \sum_{i=1}^{N} \left(I_i - \bar{I}_i \right)^2}$$

with the normalized gray level intensity of $0 \leqslant I_i \leqslant 1$, and was $C_\sigma = 0.085$ for an interrogation window of 32×32 pixel (red square). To increase the image contrast, a preprocessing was applied. First, a time filter was applied to the particle raw images subtracting the minimal intensity of each pixel of all cycles to increase the image contrast. Furthermore, a subtraction of the moving average with a window size of 12 pixel and an intensity normalization with a window size of 16 pixel was applied to each image. Figure 5 (right) shows the resulting pre-processed particle image. The image contrast within the interrogation window was increased to $C_\sigma = 0.142$.

The cross correlation for PIV was calculated with a decreasing interrogation window size from 64×64 pixels to 32×32 pixels in three iterations with a window overlap of 75%. This resulted in a mean vector spacing of about 1.0 mm. Spurious vectors with a peak ratio < 1.8 were removed and replaced iteratively using two-times median filtering with subsequent 3×3 smoothing operation.

Results

Verification of endoscopic PIV

The feasibility of endoscopic PIV in internal combustion engines was already shown.[26,27] For the verification of the endoscopic PIV the reflections, multiple-scattering of the laser and beam profile inhomogeneities have to be considered as well as the distortion and perspective errors due to endoscopic imaging. This makes a direct comparison using only one engine impossible, which is why measurements of an optical engine with identical geometry were used here for verification. Figure 6 shows the phase-averaged flow fields of the endoscopic (left) and optical engine (right) for the joint field of view. For orientation the contours of the cylinder head, the piston and the intake valves are

shown. Furthermore, an ellipse (black face) masks the part of the combustion chamber that is covered by the intake valve in the endoscopic engine. The vectors, whose length are normalized by their magnitude, indicate the flow direction and the color map the velocity magnitude. During the intake stroke at about -288°CAaTDC (top) the flow fields above y = −20 mm are in reasonable agreement regarding their direction and magnitude. Below that there are discrepancies especially on the right side where the magnitudes are higher within the optical engine and the flow is more directed towards the intake valves. During compression at about −91°CAaTDC (bottom) there is a good agreement of the velocity magnitudes and a well-formed tumble flow is found. The tumble centers are located at approximately the same position in the x-direction, whereas the tumble center in the optical engine is located about 3.5 mm higher.

A more detailed comparison is given by the profiles of the phase-averaged velocity magnitude and standard deviation in Figure 7. At −288°CAaTDC (top) the velocity magnitude of the endoscopic engine (red) and the optical engine (black) show good agreement along y = −20 mm. Along x = 0 mm, the profiles for y > −20 mm diverge and show higher magnitudes for the optical engine, whereas the standard deviations of the velocity magnitudes are nearly identical. Differences in velocity magnitude can be caused by the high-frequency oscillations of the intake manifold pressures which are different for the endoscopic and optical engine as shown in Figure 2. Welch et al.[38] found similar effects in the flow field of an optical engine and discussed it in more detail. At −91°CAaTDC the flow field of the endoscopic engine is shifted by 0.5 mm in x and 3.5 mm in y-direction. Figure 7 (bottom) shows the corresponding profiles through the tumble center coordinates y_{TC} and x_{TC}. Overall the velocity profiles agree well in magnitude and standard deviation.

The velocity differences are, with the exception of the high velocity region near the intake valves during the intake phase (−288°CAaTDC), less than 3 m/s. This is within the range of the uncertainty of the endoscopic

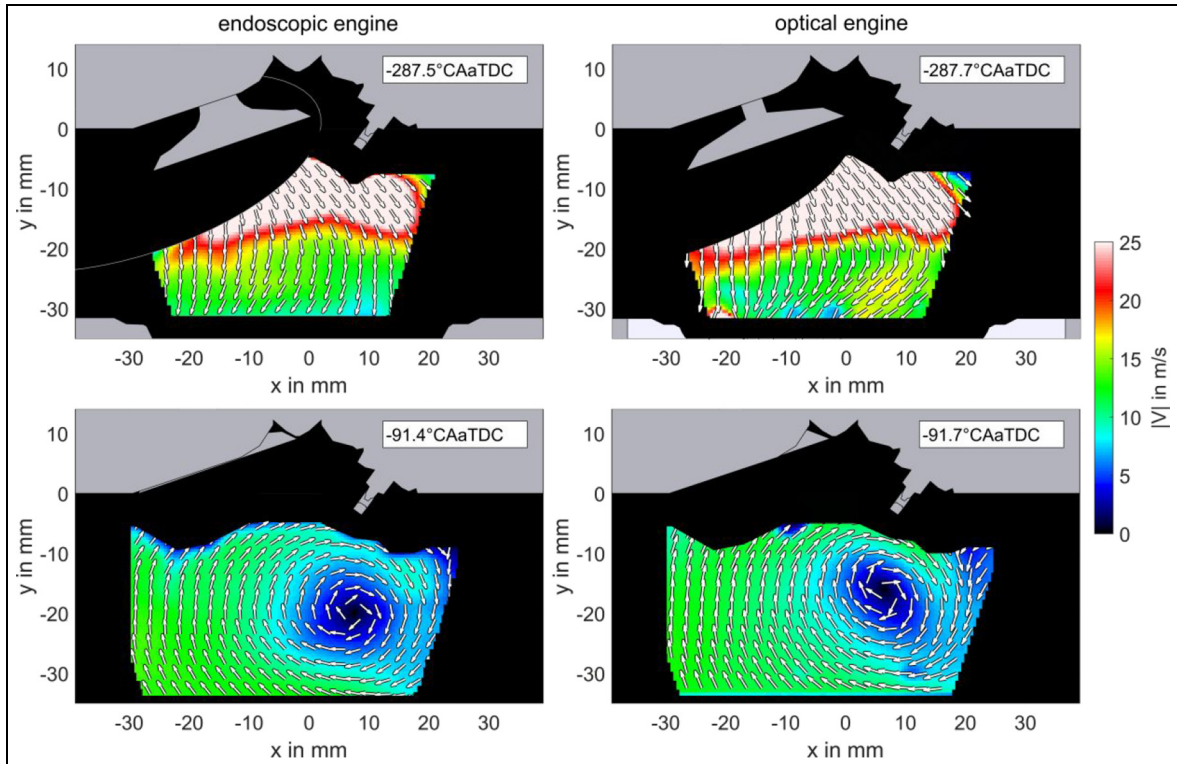**Figure 6.** Phase-averaged flow fields of endoscopic engine (left) and optical engine (right) at about -288°CAaTDC (top) and −91°CAaTDC (bottom) for the joint field of view. Length of each vector is normalized by its magnitude and velocity magnitudes are shown according to the colorbar.
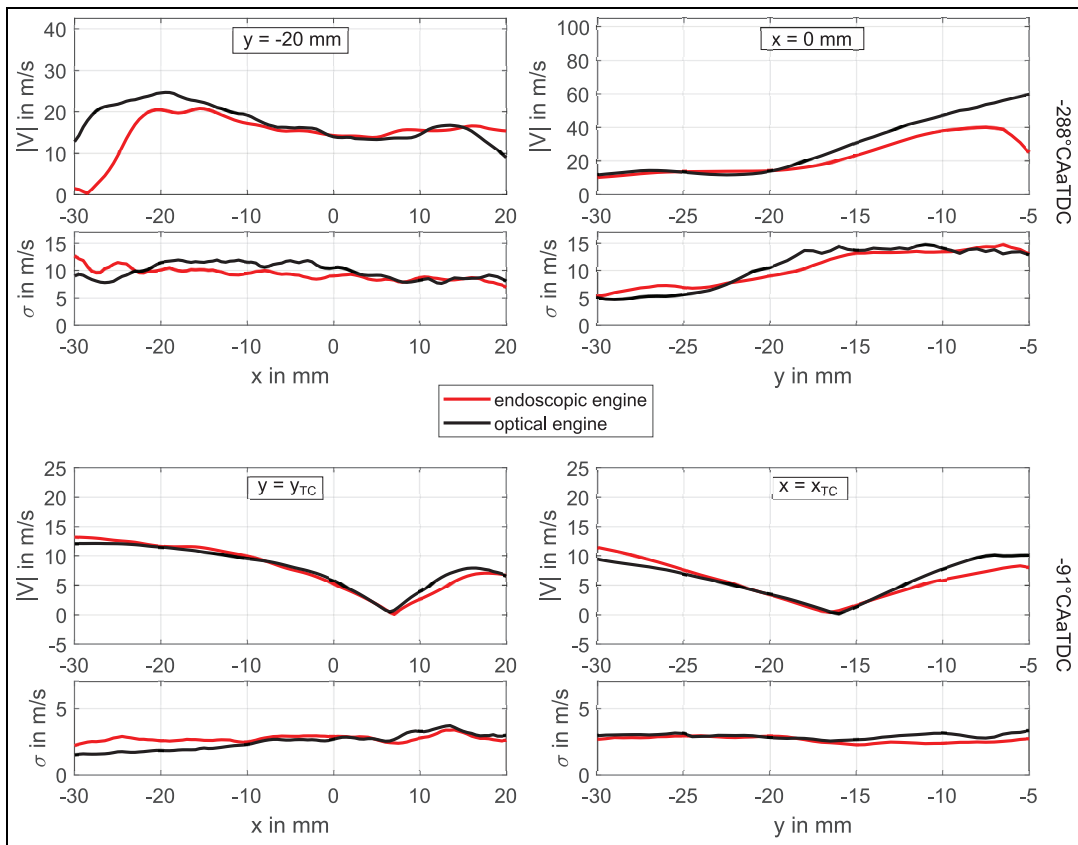

Figure 7. Profiles of the velocity magnitudes of endoscopic (red) and optical engine (black) along $y = -20$ mm (top left) and $x = 0$ mm (top right) at about $-288°$CAaTDC, and along the lines through the corresponding tumble center coordinates y_{TC} (bottom left) and x_{TC} (bottom right) at about $-91°$CAaTDC.
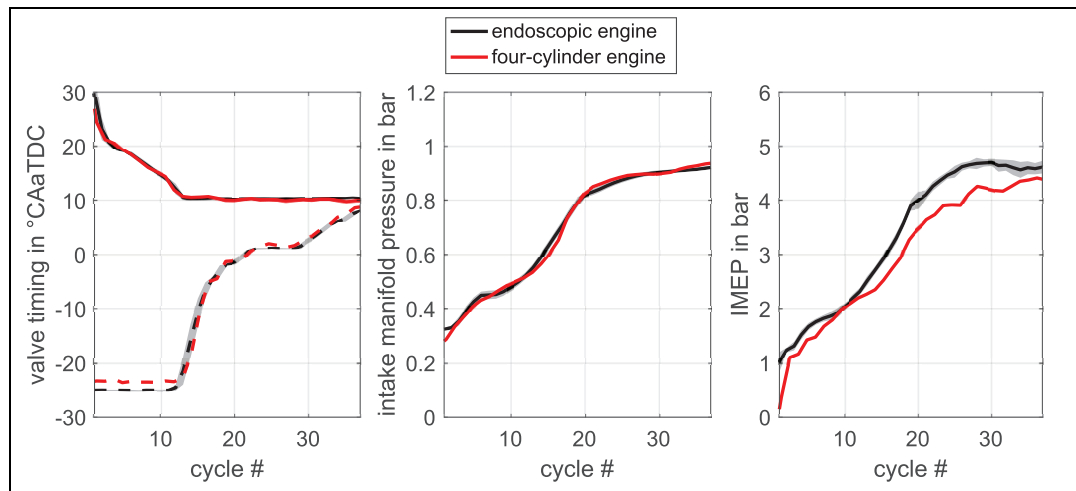
Figure 8. Valve-timings (left) of exhaust valves (dashed line) and intake valves (solid line), intake manifold pressure (middle) and IMEP (right) over the cycles along the tip-in. Averaged engine parameters of the endoscopic engine (black lines) with cycle-based deviation (gray area) and single maneuver of the four-cylinder engine (red lines).

PIV of about 0.7–2.7 m/s determined according to Wieneke.[35] Due to the angle of the endoscope to the measurement plane and the large viewing angle of 35°, the measurement represents a superposition of the in- and out-of-plane velocity components. This biases the interpretation of instantaneous flow fields compared to standard 2D PIV measurements where the influence of the out-of-plane velocity component can be neglected as described in more detail by Geis et al.,[23] Dierksheide,[27] Reeves and Lawson[32]. However, for the comparison of the phase-averaged flow fields this effect is not important, because the out-of-plane velocity component in the measured central symmetry plane is statistically zero.

Application of real transient operation

The aim of the following study was to investigate in detail the frequently observed increase of particle emissions during transient events.[6,8] A tip-in was selected which showed a significant increase in particle number emissions during the WLTC of the corresponding four-cylinder engine with the same combustion chamber geometry. The tip-in included 10 cycles of motored engine operation followed by a load-step over 37 cycles. The start of injection (SOI) was set to -290°CAaTDC for all cycles of the load-step. The maneuver was performed at an engine speed of 1400 rpm. Furthermore, a Miller cycle together with asymmetric intake valve lifts was implemented. Figure 8 shows the evolution of the valve timings (left) of the intake valves (solid line) and exhaust valves (dashed line), the intake manifold pressure (middle) and the indicated mean effective pressure IMEP (right) over the cycles of the tip-in maneuver performed on the four-cylinder engine (red lines) and applied to the endoscopic engine (black lines). Cycle 1 indicates the first cycle of the load step. While the exhaust valve timing remained unchanged at

−23°CAaTDC within the first 11 cycles, the intake valve timing was shifted from 28°CAaTDC towards the TDC of gas exchange (10°CAaTDC) to increase the amount of fresh air in the cylinder. The internal exhaust gas recirculation was increased in two steps by first shifting the exhaust valve timing to TDC in the following 10 cycles, and by a second shift starting with cycle 29. At the same time, the intake manifold pressure was increased from 0.334 bar to 0.947 bar, with the highest gradient between cycle 10 and 20. The resulting IMEP increased from about 1 bar up to more than 4 bar. Due to the Miller cycle, the turbulence intensity was reduced and 50% MFB was in the range of 5–20°CAaTDC depending on spark timing. Particle number emissions from the four-cylinder engine, divided by the number of cylinders, had peak values of about 9×10^6 #/cm^3 and the accumulated particle number emissions was about 237×10^6 #/cm^3 during the tip-in, as measured by a particle number counter (AVL APC 489).

All relevant engine parameters of the four-cylinder engine during the tip-in were applied to the endoscopic engine, such as Miller cycle strategy, valve timings, intake manifold pressure, injection, and ignition timings. This also included an air-fuel-equivalence ratio of 0.8. Since the endoscope window fouled after only a few repetitions due to soot contamination, leaner mixtures were successively applied. However, the overall evolution and sources of soot formation remained, but were reduced in total soot particle number. At an air-fuel-equivalence ratio of 1, the contamination of the endoscope was reduced sufficiently, such that several repetitions of the tip-in could be acquired. The averaged engine parameters of the endoscopic engine (black lines) were in a good agreement with those of the four-cylinder engine. Variations in the setpoint value change using the parametric table approach lead to an uncertainty of half a cycle for each engine parameter. The
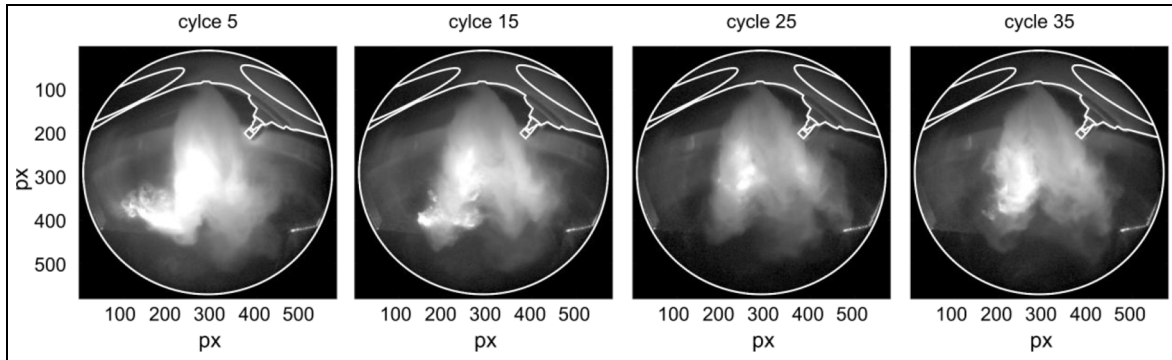
Figure 9. Instantaneous spray images at −285°CAaTDC of cycle 5, 15, 25 and 35 along the tip-in.

higher IMEP was due to the difference in the air-fuel-equivalence ratio of 0.8 in the four-cylinder engine and 1 in the endoscopic engine.

Thus, the particle number emissions measured in the exhaust of the endoscopic engine had a lower peak value in the order of 4.8×10^6 #/cm^3 and lower accumulated particle number emissions of about 121×10^6 #/cm^3. The cycle-based standard deviation of the engine parameters (gray area in Figure 7) can barely be seen indicating small fluctuations and a good reproducibility along the maneuver. The comparable particle number emissions together with the small cycle-based standard deviation of the engine parameters demonstrate that the endoscopic engine test rig is able to perform real transient engine operations with comparable particle number emissions to the four-cylinder engine.

Multi-parameter imaging during tip-in

In this section individual tip-in maneuvers applied to the endoscopic engine are examined. Endoscopic PIV, spray, flame and soot visualizations were performed simultaneously during all 37 cycles of the tip-in maneuver. The maneuver was repeated 19 times in sets of five repetitions before the front lens of the endoscope had to be cleaned. During transient engine operation, changes in engine parameters are overlapped by cycle-to-cycle variations leading to transient-to-transient variations. A single cycle analysis offers insights into different effects during individual tip-in.

Intake manifold pressure varied over a wide range during tip-in. Since the in-cylinder pressure corresponds to the intake manifold pressure when the intake valves are opened, it influences the spray formation. If the in-cylinder pressure at the start of injection is lower than the saturation vapor pressure of the injected fuel, flash-boiling may occur.[39] It was found especially during the early cycles of the tip-in, as discussed further for spray images of representative cycles. Figure 9 shows instantaneous spray images at −285°CAaTDC of cycle 5, 15, 25, and 35 along the tip-in. Spray images were not corrected for barrel distortion because the spray plumes of the 6-hole injector were outside the central symmetry plane and mostly illuminated by multiply scattered light. At an average intake manifold pressure of 0.425 bar, the spray image of cycle 5 shows a collapsed spray due to flashboiling and a strong interaction between the spray and the piston surface during the early stage of injection. With an increased average intake manifold pressure of about 0.628 bar in cycle 15 no spray collapse was observed. The spray angle continued to increase, as the spray pattern of cycle 25 shows. No further evolution of spray formation was visible in the spray pattern of cycle 35, as the average intake manifold pressure rose from about 0.875 bar in cycle 25 to 0.914 bar in cycle 35. Flashboiling occurred up to cycle 12 with an average intake manifold pressure of about 0.522 bar. Flashboiling supports the formation of fuel films on the piston surface within this cycle range, which can lead to pool fire. Since the cycle-based standard deviation of the intake manifold pressure was small for all 19 repetitions, flashboiling was found in the discussed cycle range at all repetitions of the transient.

Figures 10 and 11 show flow fields at -51°CAaTDC (left) for two single acquisitions of cycle 7 and cycle 27, respectively. In addition to the reduced flow velocity due to the Miller cycle, the asymmetric intake valve lifts lead to unstructured in-cylinder flow fields consisting of multiple small flow structures during compression. The flow fields at −51°CAaTDC show no overall directed flow structure as usually observed in high tumble SI engines. The velocity magnitude in the region of interest (red square) was below 10 m/s with an uncertainty of up to 1.6 m/s.

Figures 10 and 11 (middle and right) show the broadband detected flame and soot luminosity. Due to the three-dimensionality of the flame, the images were not corrected concerning the barrel distortion. A white balance of the images recorded with the high-speed color camera was performed using a white calibration pattern illuminated by white LEDs within the cylinder. Hence, the blue flame of the early combustion can be distinguished from the yellow to red luminosity of the soot. In addition to the cylinder head, the edge of the piston crown is shown schematically by the outer and inner curved white lines to assign the soot luminosity to pool fire.
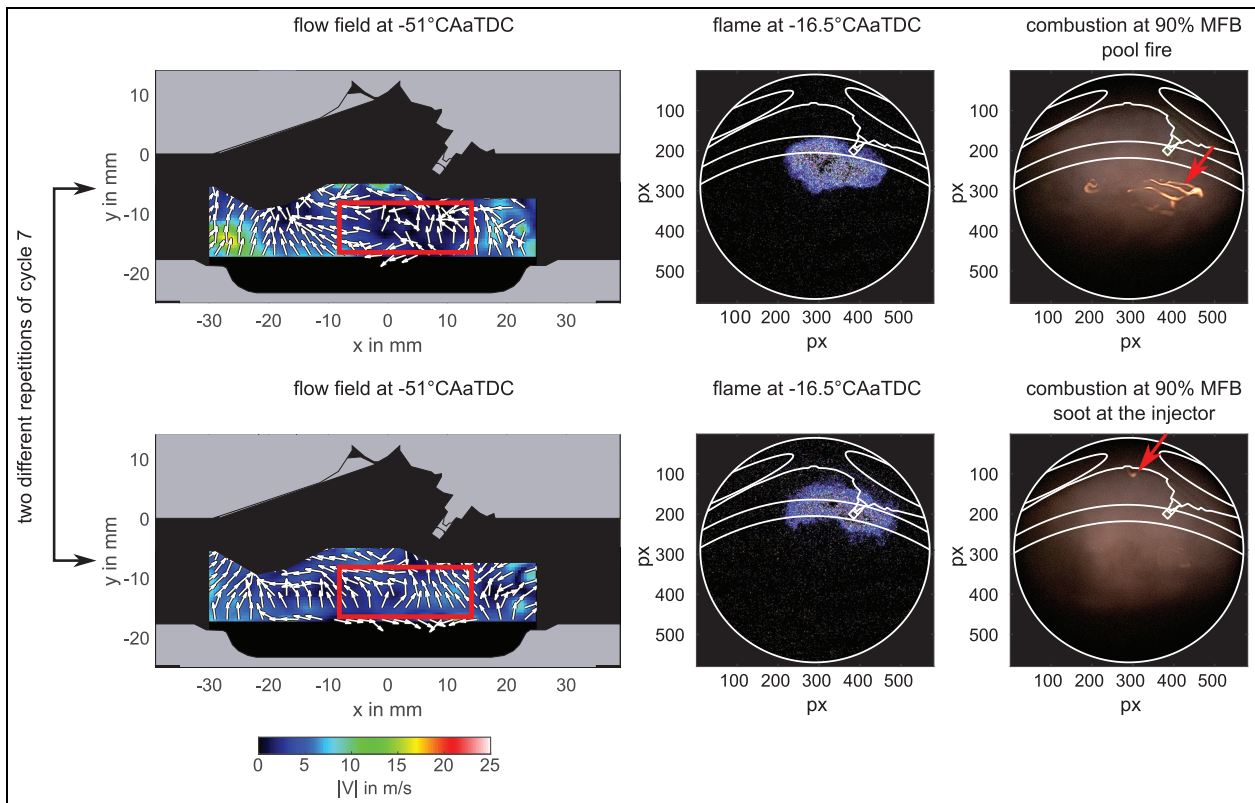
Figure 10. Flow fields at −51°CAaTDC (left), images of combustion at −16.5°CAaTDC (middle) and at 90% MFB for single acquisitions of cycle 7 from two different repetitions of the tip-in maneuvers. Vectors are normalized to their magnitude indicated by the background with velocities according to the colorbar (bottom).

In Figure 10 (top), the combustion image at −16.5°CAaTDC (20°CA after start of ignition) illustrates a flame propagating towards the intake valve and piston. The combustion image at 90% MFB shows a large diffuse weak luminosity, which is associated with soot generated in the gas phase, and a strong orange luminosity with very distinct structures on the piston surface, which is associated with pool fire. For this cycle the flow has no clear flow structure and low velocity magnitudes within the region of interest. In Figure 10 (bottom), the combustion image at −16.5°CAaTDC (20°CA after start of ignition) shows a flame propagating towards the cylinder head. This correlates with an upward directed flow which is formed beneath the spark plug within the region of interest. Furthermore, there is no pool fire in the combustion image at 90% MFB, but some soot at the injector due to fuel dripping from the injector. The combustion images at 90% MFB of cycle 7 show an overall intense soot luminosity within the gas phase for both cases but a different pool-fire behavior was observed.

A later cycle of the tip-in maneuver cycle 27 is shown in Figure 11. Figure 11 (top) shows a flow field directed towards the piston and the intake valves in the region of interest (red rectangle). In the combustion image at −12°CAaTDC (20°CA after start of ignition), the flame propagates in the same direction as the flow field as its highest intensities are in the middle of the combustion chamber above the piston crown. Pool fires are visible in the combustion images at 90% MFB especially at the piston crown below the intake valves. In Figure 11 (bottom), an upward directed flow is formed below the spark plug. The flame propagates in the combustion image at −12°CAaTDC (20°CA after start of ignition) directly towards the cylinder head. In comparison to Figure 11 (top), at 90% MFB less pool fire is visible but soot forms at the injector.

The single cycle analysis of the flow field and combustion images indicate cause-and-effect chains with respect to pool fire and soot around the injector. The direction of the flow below the spark plug at −51°CAaTDC influences the direction of flame propagation. Bode et al.[40] found flow structures to influence the propagation direction of the spark and hence the early flame kernel by correlation analysis of scanning PIV and spark visualization. If fuel films form on the piston surface or at the injector, soot formation from the fuel films is enhanced by an early arrival of the flame.

Conclusion

A single cylinder DISI engine test rig was developed to investigate the in-cylinder processes during real transient engine operation. For this purpose, a single cylinder
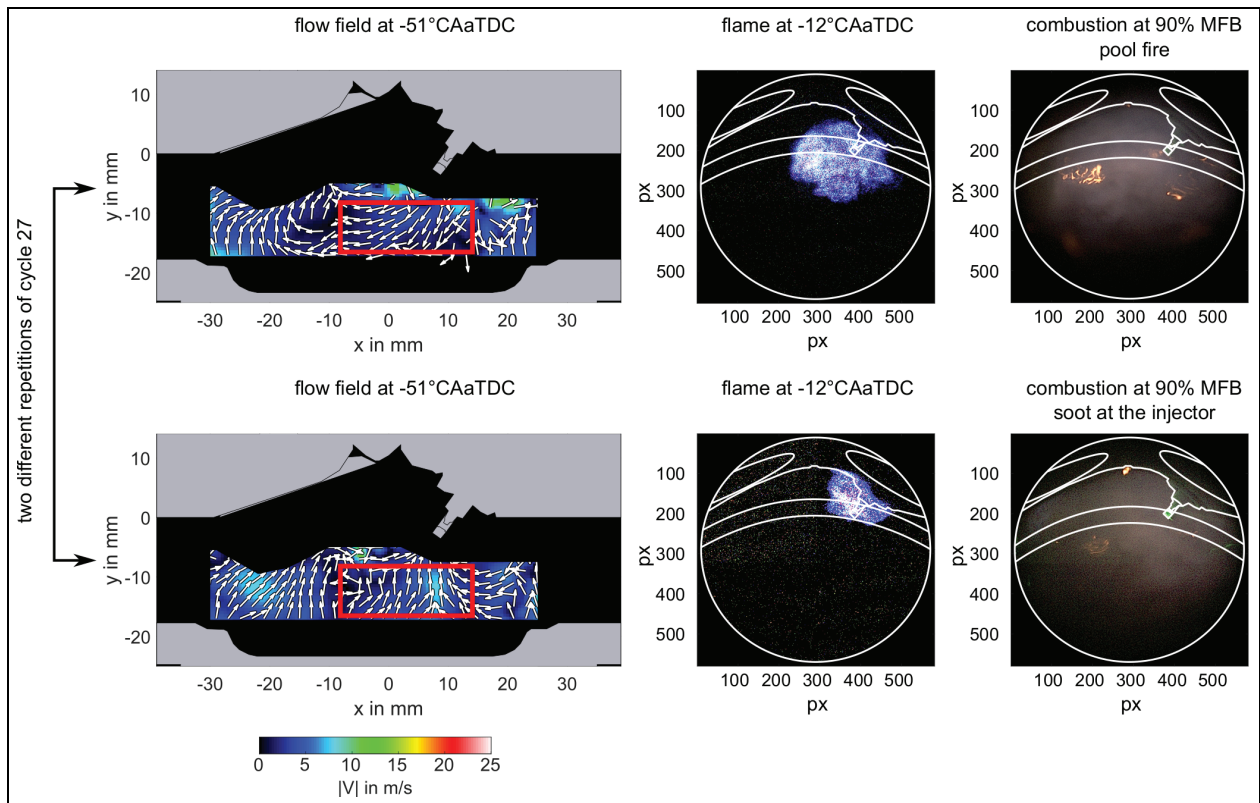
Figure 11. Flow fields at $-51°$CAaTDC (left), images of combustion at $-12°$CAaTDC (middle) and at 90% MFB for single acquisitions of cycle 27 from two different repetitions of the tip-in maneuvers. Vectors are normalized to their magnitude indicated by the background with velocities according to the colorbar (bottom).

engine with minimally invasive optical accesses with a real combustion chamber geometry was set-up. In comparison to the optical engine, a realistic engine behavior with regard to emissions, in this case soot, was demonstrated due to the omission of the large windows and the associated deep piston crevice. In addition, significantly higher loads can be realized. The engine parameters of the equivalent four-cylinder engine during a tip-in maneuver were applied to the single-cylinder engine resulting in comparable particle number emissions within the same range of several 10^6 #/cm^3. The differences in particle number emissions and IMEP were due to a different setting of the air-fuel equivalence ratio to minimize fooling of the endoscopic access. The transient-to-transient variations indicated by the cycle-based standard deviations of the engine parameter showed a good reproducibility of the tip-in.

Simultaneous endoscopic PIV, spray and combustion visualization were applied to the single cylinder engine. An oval-shaped sapphire glass window in the liner enabled laser sheet illumination in the central symmetry plane, despite unchanged piston geometry and piston rings that scraped the engine oil, used for lubrication, from the glass surface. The endoscopic PIV was verified by comparing the phase-averaged flow fields of a steady-state operating point with those of the corresponding optical engine. A good agreement was found in the structure of the flow fields and the velocity magnitudes. Together with contrast enhancing pre-

processing, a good data quality of the endoscopic PIV was found. Modifications on the test rig regarding the control of seeding density enabled endoscopic PIV during real transient engine operation.

The multi-parameter measurements during tip-in were used for a cycle-based analysis of the in-cylinder processes. By spray visualizations a collapse of the spray due to flashboiling within the first 12 cycles of the tip-in was found. The collapsed spray can be a cause for the formation of pool fires found during this part of the tip-in. Simultaneous endoscopic PIV and combustion visualization revealed cause-and-effect chains regarding the formation of pool fire on the piston and soot at the injector. The direction of the flow field below the spark plug determines the direction of flame propagation which promotes the formation of soot at the respective areas of the combustion chamber. In future work, a statistical analysis of the multi-parameter measurements will be performed to further investigate the cause-and-effect chains. In addition, a comparison of transient and steady-state operating points will be performed to analyze the effect of the transient operation on the in-cylinder processes.

Declaration of conflicting interests

The author(s) declared no potential conflicts of interest with respect to the research, authorship, and/or publication of this article.

ORCID iD

C Fach https://orcid.org/0000-0001-7279-3298

References

1. European Commission Regulation No 459/2012. *Official Journal of the European Union* 2012; L 142/16: 16–24.
2. European Commission Regulation 2017/1151. *Official Journal of the European Union* 2017; L 175/1: 1–643.
3. Peckham MS, Finch A, Campbell B, et al. Study of particle number emissions from a turbocharged gasoline direct injection (GDI) engine including data from a fast-response particle size spectrometer. SAE technical paper 2011-01-1224, 2011.
4. Peckham MS, Finch A and Campbell B. Analysis of transient HC, CO, NOx and CO_2 emissions from a GDI engine using fast response gas analyzers. *SAE Int J Engines* 2011: 1513–1522.
5. Lenz M, Cremer M, Guse D, et al. A case study on particulate emissions from a gasoline plug-in hybrid electric vehicle during engine warm-up, taking into account start–stop operation. *Proc IMechE, Part D: J Automobile Engineering* 2020; 234: 2907–2922.
6. Sabathil D, Koenigstein A, Schaffner P, et al. The influence of DISI engine operating parameters on particle number emissions. In: *SAE technical paper series*, Warrendale, PA: SAE Inernational, 2011.
7. Boulouchos K and Kirchen P. A phenomenological mean value soot model for transient engine operation. *MTZ Worldw* 2008; 69: 58–65.
8. Hadler J, Lensch-Franzen C, Gohl M, et al. Einflussfaktoren auf die Partikelentstehung unter Realfahrbedingungen. *MTZ Motortech Z* 2016; 77: 52–61.
9. Kheirkhah P, Kirchen P and Rogak S. Measurement of cycle-resolved engine-out soot concentration from a diesel-pilot assisted natural gas direct-injection compression-ignition engine. *Int J Engine Res* 2021: 146808742098626.
10. Ozdor N, Dulger M and Sher E. Cyclic variability in spark ignition engines: a literature survey. *SAE technical paper 940987*, 1994.
11. Dreher D, Schmidt M, Welch C, et al. Deep feature learning of in-cylinder flow fields to analyze cycle-to-cycle variations in an SI engine. *Int J Engine Res* 2020: 146808742097414.
12. Stiehl R, Schorr J, Krüger C, et al. In-cylinder flow and fuel spray interactions in a stratified spray-guided gasoline engine investigated by high-speed laser imaging techniques. *Flow Turbulence Combust* 2013; 91: 431–450.
13. Bode J, Schorr J, Krüger C, et al. Influence of three-dimensional in-cylinder flows on cycle-to-cycle variations in a fired stratified DISI engine measured by time-resolved dual-plane PIV. *Proc Combust Inst* 2017; 36: 3477–3485.
14. Roux B *Couplage entre simulation système et simulation aux grandes échelles pour la simulation multi-échelles de moteurs à combustion interne*. Thesis, Université Pierre et Marie Curie, Paris, 2015.
15. Disch C, Pfeil J, Kubach H, et al. Experimental investigations of a DISI engine in transient operation with regard to particle and gaseous engine-out emissions. *SAE Int J Engines* 2016; 9: 262–278.
16. Peterson B, Reuss DL and Sick V. On the ignition and flame development in a spray-guided direct-injection spark-ignition engine. *Combust Flame* 2014; 161: 240–255.
17. Peterson B, Baum E, Böhm B, et al. Early flame propagation in a spark-ignition engine measured with quasi 4D-diagnostics. *Proc Combust Inst* 2015; 35: 3829–3837.
18. Baum E, Peterson B, Böhm B, et al. On the validation of LES applied to internal combustion engine flows: part 1: comprehensive experimental database. *Flow Turbulence Combust* 2014; 92: 269–297.
19. Nicollet F, Krüger C, Schorr J, et al. A PIV-guided large-Eddy simulation of in-cylinder flows. *Oil Gas Sci Technol* 2017; 72: 28.
20. Kashdan J and Thirouard B. Optical engines as representative tools in the development of new combustion engine concepts. *Oil Gas Sci Technol* 2011; 66: 759–777.
21. Steeper RR and Stevens EJ. Characterization of combustion, piston temperatures, fuel sprays, and fuel–air mixing in a DISI optical engine. In: *International fall fuels and lubricants meeting and exposition*, Baltimore, MD: SAE International, 2016.
22. Aronsson U, Chartier C, Horn U, et al. Heat release comparison between optical and all-metal HSDI diesel engines. *SAE technical paper series, SAE International*, 2014.
23. Geis T, Rottenkolber G, Dittmann M, et al. Endoscopic PIV-measurements in an enclosed rotor-stator system with pre-swirled cooling air. In: *11th International symposium on applications of laser techniques to fluid mechanics*, Lisbon, Portugal: Calouste Gulbenkian Foundation, 2002.
24. Lemay S, Fraser R, Ciocan GD, et al. Flow field study in a bulb turbine runner using LDV and endoscopic S-PIV measurements. *IOP Conf Ser Earth Environ Sci* 2014; 22: 22015.
25. Rottier C, Godard G, Corbin F, et al. An endoscopic particle image velocimetry system for high-temperature furnaces. *Meas Sci Technol* 2010; 21: 115404.
26. Disch C, Kubach H, Spicher U, et al. Investigations of spray-induced vortex structures during multiple injections of a DISI engine in stratified operation using high-speed-PIV. *SAE technical paper series*, 2016.
27. Dierksheide U, Meyer P, Hovestadt T, et al. Endoscopic 2D particle image velocimetry (PIV) flow field measurements in IC engines. *Exp Fluids* 2002; 33: 794–800.
28. Goschütz M, Schulz C and Kaiser SA. Endoscopic imaging of early flame propagation in a near-production engine. *SAE Int J Engines* 2014; 7: 351–365.
29. Schueck C, Koch T, Samenfink W, et al. Optical investigations of soot formation mechanisms and possible countermeasures on a turbocharged port fuel injection SI engine. *SAE Int J Engines* 2016; 9: 2010–2021.
30. Hanuschkin A, Schober S, Bode J, et al. Machine learning-based analysis of in-cylinder flow fields to

predict combustion engine performance. *Int J Engine Res* 2019; 22(1): 146808741983326.

31. Adrian RJ. Particle-imaging techniques for experimental fluid mechanics. *Annu Rev Fluid Mech* 1991; 23: 261–304.

32. Reeves M and Lawson NJ. On perspective errors in endoscopic PIV. *Comptes Rendus Mécanique* 2004; 332: 687–692.

33. Tsai R. A versatile camera calibration technique for high-accuracy 3D machine vision metrology using off-the-shelf TV cameras and lenses. *IEEE J Robot Automat* 1987; 3: 323–344.

34. Willert CE. Assessment of camera models for use in planar velocimetry calibration. *Exp Fluids* 2006; 41: 135–143.

35. Wieneke B. PIV uncertainty quantification from correlation statistics. *Meas Sci Technol* 2015; 26: 74002.

36. Guezennec YG and Kiritsis N. Statistical investigation of errors in particle image velocimetry. *Exp Fluids* 1990; 10: 136–146.

37. Peli E. Contrast in complex images. *J Opt Soc Am A* 1990; 7.

38. Welch C, Schmidt M, Keskinen K, et al. The effects of intake pressure on in-cylinder gas velocities in an optically accessible single-cylinder research engine. *SAE technical paper series, SAE International*, 2021.

39. Schulz F and Beyrau F. The influence of flash-boiling on spray-targeting and fuel film formation. *Fuel* 2017; 208: 587–594.

40. Bode J, Schorr J, Krüger C, et al. Influence of the in-cylinder flow on cycle-to-cycle variations in lean combustion DISI engines measured by high-speed scanning-PIV. *Proc Combust Inst* 2019; 37: 4929–4936.